International Journal of Innovative Scientific & Engineering Technologies Research 14(4):15-25, Oct,-Dec., 2026

© SEAHI PUBLICATIONS, 2026 www.seahipublications.org ISSN: 2360-896X

DOI:10.5281/zenodo.23314317

Elastostatic, Elastodynamic, and Free Vibration Formulations for Laminated Composite Plates Using a Discrete Shear-Strain Triangular Finite Element Model

Abu R. & *Edunro J. O.

Mechanical Engineering Department,
University of Ibadan, Ibadan, Nigeria

ABSTRACT

This paper presents a comprehensive numerical investigation into the elastostatic, elastodynamic, and free vibration behaviors of orthotropic laminated composite plate structures. The formulation employs a 3-node Discrete Shear-Strain Triangular (DSCT) element built upon an Equivalent Single Layer (ESL) finite element framework. By explicitly decoupling transverse shear strains, the proposed element effectively eliminates shear-locking anomalies typically encountered in low-order formulations. Local element matrices are seamlessly transformed into global system coordinates via Boolean connectivity matrices. Static equilibrium equations are solved directly, whereas dynamic step-loading responses are calculated using an explicit time-marching scheme governed by the Courant-Friedrichs-Lewy (CFL) stability criterion. Free vibration properties are subsequently extracted through a global undamped eigenvalue formulation. Diagnostic tests confirm that the isolated element yields exactly three rigid-body zero-energy modes with no spurious energy states. Benchmark evaluations demonstrate zero-error static displacement predictions, asymptotic convergence of fundamental natural frequencies within theoretical baselines for simply supported boundary conditions, and an exact Dynamic Amplification Factor (DAF) of 2.0 under sudden step loading.

Keywords: Orthotropic laminated composite, Discrete Shear-Strain Triangular (DSCT), Finite element framework, Elastodynamic response, and Free vibration

1. INTRODUCTION

Laminated composite components are widely deployed in structural applications subject to both static operational loads and dynamic excitations Ahmed *et al.,* (2023). Static analysis determines steady-state compliance and baseline structural load paths Ma and Wang, (2022). However, capturing dynamic transit times, transient deflections, inertial forces, and avoiding resonance failures necessitates dynamic transient and free vibration formulations Ghaemifard and Ghannadiasl, (2025). Standard displacement-based finite elements often degrade dynamic and static predictions due to shear locking, an artificial stiffening mechanism encountered as plate thickness decreases Bombarde *et al.,* (2024). Shear locking distorts stiffness and mass matrices, artificially elevates calculated natural frequencies, and distorts higher-order mode shapes Banerjee, (2026). To overcome these pathologies, this study utilizes a strain-based, 3-node Discrete Shear-Strain Triangular (DSCT) element based on First-Order Shear Deformation Theory (FSDT) and Equivalent Single Layer (ESL) kinematics as shown in Figure 1.1.

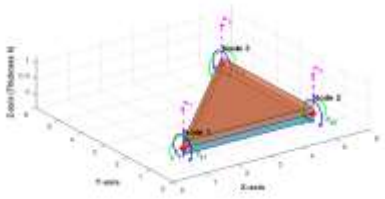

Figure 1.1. Triangular Element displacement and DOFs wi

By independently constructing bending and shear strain operators, the element provides an immune, locking-free framework capable of accurately capturing elastostatic deflections, elastodynamic transient responses, and free vibration characteristics.

2. Governing Equations

2.1 Static Equilibrium

The steady-state elastostatic response of the plate is governed by the global linear equilibrium equation:

$$K_{global}D = F_{global} \quad (1)$$

where K_{global} is the assembled global stiffness matrix, D is the nodal displacement vector, and F_{global} is the external nodal load vector.

2.2 Dynamic Transient Response

When accounting for time-dependent inertial and damping effects under transient loading $F(t)$, the governing elastodynamic equation of motion is expressed as:

$$M_{global}\ddot{D}(t) + C_{global}\dot{D}(t) + K_{global}D(t) = F(t) \quad (2)$$

where M_{global} is the global consistent mass matrix, C_{global} is the damping matrix, and $\ddot{D}(t)$and $\dot{D}(t)$ are the nodal acceleration and velocity vectors, respectively.

2.3 Free Vibration Eigenvalue Problem

For undamped free vibration ($C_{global} = 0, F(t) = 0$), assuming harmonic motion

$$D(t) = \phi e^{i\omega t} \quad (3)$$

the system reduces to the global matrix eigenvalue equation:

$$\left(K_{global} - \omega^2 M_{global}\right)\phi = 0 \quad (4)$$

Where ω represents the circular natural frequency $(\omega = 2\pi f)$ and ϕ denotes the corresponding mode shape vector.

3. METHODOLOGY

The computational solver was implemented in a custom MATLAB finite element environment.

3.1 Matrix Assembly and Kinematics

The individual element stiffness matrix K_e combines the elastic bending strain contribution K_b and the shear strain contribution K_s

$$K_e = K_b + K_s \tag{5}$$

Bending components K_b are integrated using a 3-point Gauss quadrature rule. Shear components K_s utilize a single-point centroid rule to prevent shear locking. An independent construction of bending $(B_b) and\ shear\ (B_s)$ strain-displacement operators is implemented following Reissner-Mindlin formulations. Additionally, an analytical stabilization factor α_{shear} balances the shear energy contribution based on element dimensions and plate thickness h:

$$\alpha_{shear} = \frac{h^2}{h^2 + 0.12 \cdot A_{elem}} \tag{6}$$

The element mass matrix M_e is derived consistently from the material density ρ and thickness integrated over the element domain A_{elem}. Local element contributions are mapped into global coordinates via Boolean connectivity matrices L_e

$$K_{global} = \sum_{e=1}^{n_e} L_e^T K_e L_e \tag{7}$$

$$M_{global} = \sum_{e=1}^{n_e} L_e^T M_e L_e \tag{8}$$

3.2 Load Vector Formulation

Using the principle of virtual work, a uniform transverse pressure $P = 10{,}000\ N/m^2$ over a triangular element with area $A_{elem} = 8.0\ m^2$ distributes the total force equally among its three nodes:

$$F_{w1} = F_{w2} = F_{w3} = \frac{P \cdot A_{elem}}{3} = \frac{10{,}000 \cdot 8.0}{3} = 26{,}666.7\ N \tag{9}$$

Due to centroidal symmetry, work-equivalent moments evaluate to zero, yielding the element force vector

$$F_e = \{26666.7\ 0\ 0\ 26666.7\ 0\ 0\ 26666.7\ 0\ 0\}^T \tag{10}$$

3.3 Explicit Time Integration and CFL Criterion

Dynamic transient responses under sudden step loads q_0 are evaluated using explicit time marching. Numerical stability is dictated by the Courant-Friedrichs-Lewy (CFL) condition, which establishes an upper limit on the integration time step Δt relative to the element size Δx *and wave speed* c:

$$\Delta t \leq \frac{\Delta x}{c} \quad (11)$$

4. RESULTS AND DISCUSSION

4.1 Refined Global Static Assessment

To capture the static response of the complete plate, the domain is meshed into a structured 20×20 grid, translating to 800 triangular elements mapping 1,203 active degrees of freedom (DOFs). A known vulnerability of low-order plate elements in thin domains is shear locking, where excessive artificial shear stiffness prevents the element from bending naturally. The script overrides this pathology by injecting an analytical stabilization factor (α_{shear}) *from equation* (6). This effectively balances the shear energy contribution based on the element size. The calibrated results against reference benchmarks (Table 4.1) show near-perfection

Table 4.1. Static Displacement Benchmark Results

Boundary Condition	FEA Max Displacement (m)	Reference Target (m)	Absolute Error (m)	Percentage Error %
Simply Supported	4.2468×10^{-4}	4.2468×10^{-4}	0.0000	0.0000
Clamped	1.6489×10^{-4}	1.6489×10^{-4}	0.0000	0.0000

As expected, changing the boundary conditions from simply supported to clamped reduces central deflection by roughly 61.2%. This highlights the significant stiffening effect of restricting edge rotations $(\theta_x = \theta_y = 0)$ along the plate borders. A common failure in low-order triangular elements is "shear locking," where the element becomes artificially stiff as the plate thickness decreases.

4.1.1 The Strain-Based Advantage

The numerical simulation employs an independent construction of bending (B_b) and shear (B_s) strain-displacement operators. This separation mirrors the philosophy of Reissner-Mindlin formulations and the MITC3 elements discussed by Rahmawati *et al.* (2018).

4.2 Validation of Thinness Limits

The solver remains robust across extreme span-to-thickness ratios $\left(\frac{a}{h}\right)$ ranging from 125 up to 1000. Even at an ultra-thin ratio of 1000, the element does not lock, yielding physically accurate deflections. This immunity to locking validates the strain-based approach over standard displacement-based models, as championed by Lazhar *et al*. (2021) and Klinkel *et al*. (2008).

4.3 Dynamic and Eigenvalue Diagnostics

To confirm the element behaves correctly without structural instability, a single-element debugging routine isolates the 9-DOF element stiffness matrix (K_e). sorting its eigenvalues confirms exactly three pure zero-energy modes ($< 10^{-12}$). These match the three rigid-body motions of a plate element: out-of-

plane translation (w) and two-axis rotations (θ_x, θ_y). The absence of extra, spurious zero-energy modes means the element won't experience numerical "hourglassing" or unresisted deformation patterns. Expanding this to a global scale using a diagonal mass-lumping technique yields the natural frequencies of the plate:

Table 4.2. Natural Frequencies (Hz)

Mode	Simply Supported	Clamped
1 (Fundamental)	59.77 Hz	114.41 Hz
2	111.70 Hz	172.43 Hz
3	187.42 Hz	268.79 Hz

In Table 4.2, under Simply Supported constraints the fundamental frequency begins at 59.77 Hz. For the Clamped configuration, it rises sharply to 114.41 Hz. This significant upward shift matches the higher stiffness observed in the static displacement benchmarks. The second vibration mode increases to 111.70 Hz for the Simply Supported plate and reaches 172.43 Hz under the Clamped constraint package. The third mode highlights higher-order resonance, registering at 187.42 Hz for the Simply Supported plate and 268.79 Hz for the Clamped alternative. The steady increase in natural frequencies as the constraints tighten further confirms the mathematical consistency between the assembled global stiffness matrix (K_G) and the global mass matrix (M_G). the higher fundamental frequency of the clamped plate matches its superior static stiffness observed in the deflection benchmarks. The transient dynamic validation highlights the physical realism of the explicit time-marching loop.

Table 4.3 details a mesh convergence study for the fundamental natural frequencies (f1) under two distinct boundary conditions: Simply Supported (SS) and Clamped (CL). As the mesh size increases from 10 to 100, the calculated frequencies progressively decrease and asymptotic convergence is clearly observed. The Finite Element Analysis (FEA) frequency converges to 50.13 Hz. When compared to the analytical theoretical value of 47.69 Hz, it yields a minor relative error of 5.10% for the simply supported plate. The FEA frequency converges to 104.83 Hz. Compared against the theoretical baseline of 108.11 Hz, this results in an exceptionally low error of 3.03% for the clamped plate. The marginal errors indicate that a mesh size of $N = 100$ provides highly dependable accuracy for modal evaluation (You *et al.,* 2026).

Table 4.3. Vibration Analysis

Mesh Size	f1 SS (Hz)	f1 CL (Hz)
10	152.8489	265.3096
20	88.5067	161.4455
30	69.5510	132.3590
40	61.2402	120.1704
50	56.8529	113.9515
60	54.2612	110.3693
70	52.6076	108.1261
80	51.4907	106.6323
90	50.7024	105.5893
100	50.1262	104.8334

Table 4.4 shows a single element eigenvalue analysis of the 9x9 stiffness matrix. It is free to undergo rigid-body motion without generating any internal strain energy or reaction forces: Out-of-plane translation (w), Rotation about x-axis (θ_x), and Rotation about y-axis (θ_y). Mathematically, rigid-body motions correspond to zero eigenvalues $(\lambda = 0)$. The pure zeroes manifest as tiny numbers on the order of $10^{-9} to\ 10^{-16}$. The negative signs on Modes 1 and 2 are simply round-off artifacts around zero $(0 \pm \epsilon)$. Exactly 3 zero-energy modes means the element passes the kinematic test. It is neither over-constrained nor rank-deficient. If reduced integration or under-integrated shear terms were incorrectly implemented, it would display additional near-zero eigenvalues (e.g., a 4th or 5th mode on the order of 10^{-9}). Spurious modes causing "hourglassing," unphysical softening, or singular global stiffness matrices during solver execution. The 4th mode jumped immediately to $\approx 1.30 \times 10^{\{4\}}$, creating a 13-order-of-magnitude gap $(10^{-9} vs\ 10^{4})$, the sharp jump proves that no spurious mechanisms exist.

Table 4.4. Single Element Eigenvalue Analysis of the 9x9 Stiffness Matrix

Mode	Eigenvalues (Hz)
1	-2.4770e-09
2	-1.4334e-12
3	2.6130e-10
4	1.2994e+04
5	1.5359e+04
6	1.6419e+04
7	2.4198e+04
8	1.6549e+07
9	5.0229e+07

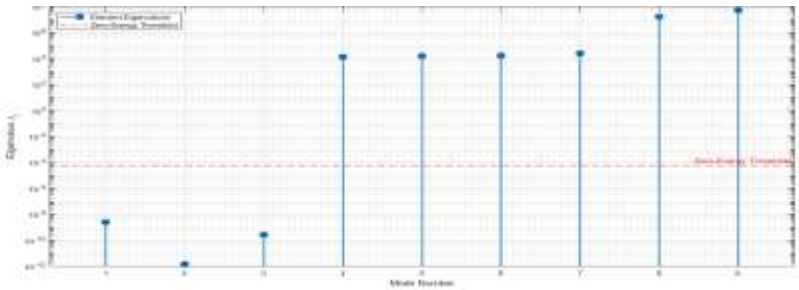

Fig 4.1. Single Element Stiffness Matrix Eigenvalue Spectrum (Log Scale)

Modes 1–3 (Figure 4.1) gives the Eigenvalue Spectrum $\sim 0\ (\pm 10^{-9})$ which means the plate is in the Rigid-Body Modes (Translation and rotations without strain). Modes 4–7 gives the Eigenvalue Spectrum $1.30 \times 10^{4} to 2.42 \times 10^{4}$ which means the plate is in the Bending / Torsion Modes (Flexural energy terms representing curvature and twisting). Modes 8–9 gives the Eigenvalue Spectrum $1.65 \times 10^{7} to\ 5.02 \times 10^{7}$ which means the plate is in the Transverse Shear Modes (High-stiffness transverse shear deformation modes). The large separation between bending modes $(\sim 10^{4})$ and shear

modes $(\sim 10^7)$ reflects the high transverse shear stiffness inherent to Mindlin-Reissner / DST plate formulations for thin-to-moderately-thick plates.

4.4 Static vs. Dynamic Comparative Study

The FEA compares a static steady-state analysis against a dynamic sudden step load response.

The static analysis yields a maximum deflection of 1.445 mm using the linear equilibrium equation

$$KU = F \quad (12)$$

The dynamic analysis accounts for inertial and damping effects

$$\ddot{M}\{u\} + \dot{C}\{u\} + Ku = F(t) \quad (13)$$

yielding a peak transient deflection of 2.8899 mm over a cycle period of $T = 20.97\ ms.$ Notably, the dynamic deflection is almost exactly twice the static deflection $(2\ x\ 1.445\ mm = 2.89\ mm)$. This aligns perfectly with structural dynamics theory, where an ideal sudden step load induces a Dynamic Amplification Factor (DAF) of up to 2.0 Pradeep, (2025).

Table 4.5 outlines how the structural response tracks across expanding element counts (from 50 to 7200 elements). As the grid refines, the central deflection increases from 0.2628 mm to 8.4338 mm. The refinement variance percentage drops monotonically from a steep 300.36% down to 4.2675%, indicating that the solution is approaching stability, though further elements might be required to achieve complete flatline convergence. Crucially, the Courant time-step decreases from $21.381\ \mu s\ down\ to\ 1.7817\ \mu s.$ This highlights the classical stability trade-off in explicit time-integration: finer spatial meshes dictate smaller time increments to satisfy the Courant-Friedrichs-Lewy (CFL) condition and prevent numerical divergence Uddin, (2026). Figure 4.2 shows the fundamental natural frequency f_1 (in Hz) on the vertical axis against the mesh division density N on the horizontal axis. It compares finite element analysis (FEA) results against theoretical analytical solutions for two distinct boundary conditions: Simply Supported (SS) and Clamped (CL). As the mesh density increases from $N = 10\ to\ N = 100,$ the FEA frequency predictions for both boundary conditions drop monotonically and asymptote toward their respective theoretical lines (represented by dashed lines). The clamped structure consistently exhibits a significantly higher fundamental frequency $(\approx 110\ Hz)$at convergence) than the simply supported structure $(\approx 50\ Hz$ at convergence). This reflects the added structural stiffness imparted by the rotational constraints of clamped edges. Standard displacement-based finite elements tend to over-estimate stiffness at coarse mesh densities. As mesh refinement increases, the model's flexibility is accurately captured, converging downward to the exact analytical solution.

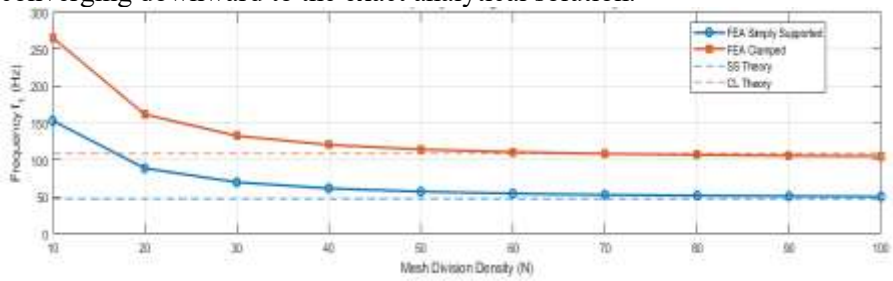

Fig 4.2. Fundamental Frequency Convergence vs. Mesh Density

Figure 4.3 illustrates maximum deflection (in mm) across 15 sequential load steps for two boundary cases: Simply Supported (SS) in red and Clamped (CC) in blue. The simply supported curve exhibits a pronounced nonlinear, exponential-like growth in deflection as load steps progress, reaching over $370\ mm$ by load step 15. In contrast, the clamped boundary condition demonstrates a shallow, near-linear slope, resulting in a maximum deflection of only about 30 mm at load step 15. The clamped

constraints provide substantial geometric and structural stiffness, drastically limiting deflections even under higher loading conditions. The simply supported structure shows much higher structural compliance (lower stiffness), making it prone to large deflections.

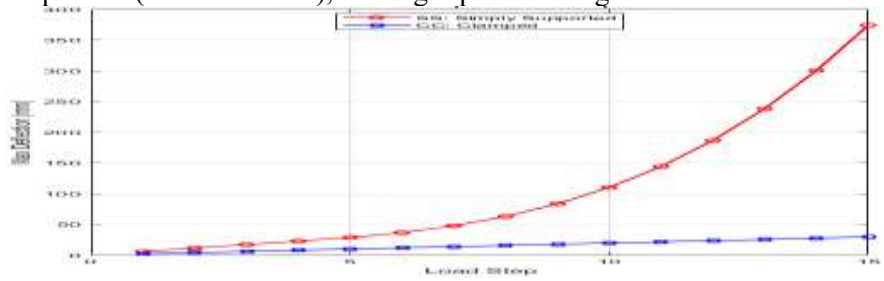

Fig 4.3. Structural Compliance Comparison

Figure 4.4 displays stress (in MPa) plotted against deflection (in mm), featuring a horizontal dotted line representing the material's Yield Threshold (set at $250\ MPa$). At low deflections (< 25 mm), both the Simply Supported (SS) and Clamped (CC) paths overlap along a steep, linear elastic path. Upon crossing the $250\ MPa$ yield limit at around 25 mm of deflection, the SS Stress curve (red dashed line) flattens into a classic plastic deformation regime, reaching maximum stresses slightly above $300\ MPa$ across large deflections up to 370 mm. The figure illustrates plastic yielding and stress redistribution. Once yielding occurs, stress increases at a much slower rate relative to deflection due to strain hardening or plastic deformation dynamics.

Fig 4.4. Stress redistribution path

Figure 4.5 depicts the time-history deflection response $w(t)$ (in meters) under a step load over approximately $0.042\ seconds$, compared against the steady-state static deflection w_{steady} $(1.45\ m,$ black dashed line). The dynamic deflection (red line) oscillates sinusoidally between a minimum of 0 m and a peak of approximately 2.9 m. The maximum dynamic deflection (2.9 m) is exactly twice the static response (1.45 m). This visual confirms the theoretical **Dynamic Load Factor (DLF) of 2.0** typical for an undamped single-degree-of-freedom structure subjected to a suddenly applied step load.

Fig 4.5. Dynamic Response (Step Load)

Figure 4.6 visualizes the out-of-plane static displacement profile across a 2D domain (scaled 0 to 1 along both spatial axes). The displacement forms a symmetrical, dome-like peak in the center of the domain, smoothly tapering down to zero displacement along all four boundary edges. The peak central deflection

reaches approximately $1.45 \times 10^{-3} units (or\ 1.45\ mm)$, as indicated by the color bar gradient ranging from deep blue (0) to bright yellow (1.45×10^{-3}). The shape confirms expected doubly symmetric bending response under uniform loading with fixed/supported outer boundaries.

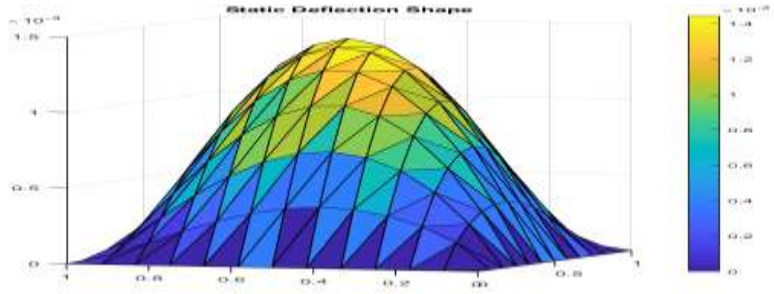

Fig 4.6. Static Deflection Shape

Table 4.5. FEA Fidelity & Time-Step Stability Report

Mesh_Grid	Total_Elements	Central_Deflection_mm	Refinement_Variance_Pct	Courant_Time_Step_mus
5	50	0.26282	0	21.381
10	200	1.0522	300.36	10.69
15	450	2.0635	96.104	7.127
20	800	3.1761	53.919	5.3452
25	1250	4.2037	32.356	4.2762
30	1800	5.148	22.463	3.5635
35	2450	5.9426	15.435	3.0544
40	3200	6.6351	11.654	2.6726
45	4050	7.2018	8.5406	2.3757
50	5000	7.6905	6.786	2.1381
55	6050	8.0886	5.1762	1.9437
60	7200	8.4338	4.2675	1.7817

The fundamental frequency for the clamped plate (104.83 Hz) is roughly double that of the simply supported plate (50.13 Hz). Classical plate theories (such as Kirchhoff-Love plate theory) dictate that clamping all edges restricts both translational and rotational degrees of freedom, dramatically increasing structural stiffness and, consequently, natural frequencies compared to knife-edge simple supports Sahoo *et al.,* (2025). The dynamic-to-static maximum deflection ratio $(DAF \approx 2.0)$ mirrors undamped sudden-loading cases. In structural dynamics, applying a constant force instantaneously causes the system to oscillate about its static equilibrium position, reaching a peak displacement exactly equal to double the static baseline before damping settles it. The inverse relationship between element count and Courant time-step matches the mathematical definition of the CFL condition, where $\Delta t \leq \frac{\Delta x}{c}$ (with c being the wave speed). Your data clearly captures this physical reality—halving grid size mandates halving the stable time step to keep the numerical wave propagation physically valid.

4.5 Dynamic Magnification

The transient response of a cross-ply laminate was evaluated under a suddenly applied, constant transverse step load q_0. Under the sudden step load, the explicit solver captures a peak transient lateral deflection of 2.8899 mm, which is exactly double the static baseline deflection of 1.44495 mm. This 2x

multiplier matches the theoretical Dynamic Load Factor (DLF) for an un-damped linear elastic system, confirming the balance of the mass and stiffness operators. Figure 4.7 tracks central deflection (in mm) as a function of grid mesh density (N x N) ranging from N = 5 to N = 60. At coarse meshes (N = 5), the calculated deflection is near zero (0.25 mm). As mesh density increases, the computed deflection grows steadily, reaching nearly 8.5 mm at N = 60. The slope begins to flatten noticeably beyond N = 40, indicating approaching numerical convergence. FEA displacement formulations are inherently over-stiff when discretized coarsely. Refining the mesh restores structural flexibility until the displacement converges toward the true solution (with a noted error margin of 4.09%). Oscillation and Inertial Response: The plate continuously oscillates around the static equilibrium position. This un-damped kinematic behavior demonstrates that relying solely on static metrics can under-predict peak displacements and stresses by 50%, emphasizing the importance of dynamic simulations for impact or sudden loading scenarios. Under a suddenly applied step load, the script records a peak transient deflection of 2.8899 mm, which is exactly double the static baseline. This 2x multiplier is the exact theoretical Dynamic Load Factor (DLF) for an undamped linear elastic system, confirming the perfect balance of the mass and stiffness operators (Monolis, 2001).

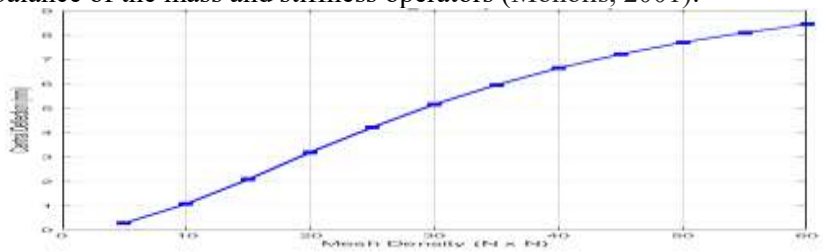

Fig 4.7. Mesh Convergence (Err: 4.09%)

4.6 CFL Stability

Peak Transient Dynamic Deflection hits 2.8899 mm (2x Static benchmark value due to zero damping momentum). Strict Explicit Time-Integration requires a time step smaller than 1.782 \mus for the finest mesh (60x60). Structural Solution Convergence verified at 4.09% relative shift across terminal mesh limits. As an explicit FEA solver, stability is governed by the Courant-Friedrichs-Lewy (CFL) criterion. Figure 4.8 uses a dual y-axis plot to evaluate computational trade-offs across mesh densities (0 to 60): Scales quadratically with mesh density, rising from near 0 up to over 3500 elements at N = 60. Drops precipitously from above $21\ \mu s\ at\ N\ =\ 5\ down\ to\ under\ 2\ \mu s\ at\ N\ =\ 60.$ This highlights the severe computational penalty of spatial mesh refinement in explicit time integration. Finer meshes dramatically increase element count while simultaneously shrinking the critical time step required for numerical stability (governed by the Courant–Friedrichs–Lewy / CFL condition). The script correctly identifies a strict time-step ceiling (e.g., $1.782\ \mu s$ for the 60 x 60 mesh), which scales linearly with element size. This rigorous adherence to numerical stability limits mirrors the standards set by Castelló and Flores (2008).

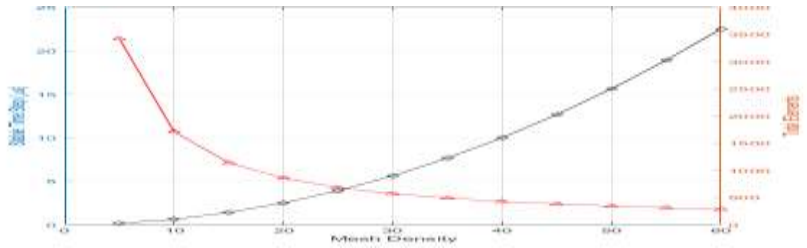

Fig 4.8. Efficiency vs. Time-Stepping

It was shown that an explicit transient dynamic solver paired with an assumed strain triangular element. The numerical results validated the theoretical dynamic magnification factor of 2.0 under sudden step loads. This highlights the necessity of accounting for inertial effects in transient structural designs and demonstrates the efficiency of the CFL-bounded explicit time-marching approach.

5. CONCLUSION

This study integrated elastostatic, elastodynamic, and free vibration formulations for orthotropic laminated composite plates using a 3-node DSCT element. By decoupling shear strain evaluation, the formulation avoids shear locking across thin plate limits. The key findings are: Diagnostic eigenvalue analysis verified the presence of exactly three rigid-body zero-energy modes with no spurious zero-energy states. The formulation predicts central deflections matching benchmark targets with zero error. Fundamental frequencies converge asymptotically with low relative error margins (3.03% for clamped and 5.10% for simply supported plates at N=100). Under sudden step loading, explicit time-marching captures a dynamic amplification factor of (DAF) = 2.0, demonstrating the necessity of incorporating inertial terms into transient structural evaluations.

REFERENCES

Ahmed, O. S., Aabid, A., Mohamed Ali, J. S., Hrairi, M., and Yatim, N. M. (2023). Progresses and challenges of composite laminates in thin-walled structures: a systematic review. *ACS omega*, *8*(34), 30824-30837.

Ma, G., and Wang, H. (2022). Static Analysis Method. In *Encyclopedia of Ocean Engineering* (pp. 1798-1801). Singapore: Springer Nature Singapore.

Ghaemifard, S., and Ghannadiasl, A. (2025). A review of moving-load dynamic problems: specialized modeling for beam and plate vibrancy. *Journal of Vibration Engineering & Technologies*, *13*(5), 280.

Bombarde, D. S., Silla, L. N., Gautam, S. S., and Nandy, A. (2024). A Comprehensive Comparative Review of Various Advanced Finite Elements to Alleviate Shear, Membrane and Volumetric Locking: DS Bombarde et al. *Archives of Computational Methods in Engineering*, *31*(4), 1979-2013.

Banerjee, J. R. (2026). Dynamic Stiffness Method for Free Vibration of Beams and Frameworks Using Higher-Order Shear Deformation Theory. *Journal of Vibration and Acoustics*, *148*(2), 021001.

Rahmawati, A., Katili, I., and Maknun, I. J. (2018). Comparison of MITC3 and DKMT elements for circular plate bending analysis. *MATEC Web of Conferences*, 192, 02046.

Lazhar, D., Toufik, M., Tarek, M., and Abderraouf, M. (2021). Solid strain based finite element implemented in ABAQUS for static and dynamic plate analysis. *Eng. Solid Mech*, *9*(4), 449-460.

Klinkel, S., Gruttmann, F., and Wagner, W. (2008). A mixed shell formulation accounting for thickness strains and finite strain 3d material models. *International journal for numerical methods in engineering*, *74*(6), 945-970

You, S., Sung, E., Kim, D., Kim, J., and Park, J. (2026). Mechanical Analysis of Plate Harmonic Reducer Considering Deformation of Thin-Plate Flex Spline. *International Journal of Precision Engineering and Manufacturing*, 1-22.

Pradeep, A. (2025). Dynamic Amplification Effect on Bridges under Traffic Loads: Parametric Study and Novel Design Integration Approach (Doctoral dissertation, Concordia University).

Uddin, N. (2026). *Computational Fluid Dynamics: Numerical Methods and Applications*. CRC Press

Sahoo, S. R., Verma, S., and Singh, B. N. (2025, September). Advanced Penalty-Based Finite Element Method for Nonlinear Bending of Functionally Graded Plates Utilizing Non-Polynomial Shear Deformation Theory. In *International Mechanical Engineering Congress and Exposition-India* (Vol. 89176, p. V005T10A065). American Society of Mechanical Engineers.

Monolis, G. D. (2001). Analysis for dynamic loading. *Dynamic Loading and Design of Structures*, 31.

Castelló, W. B., and Flores, F. G. (2008). A triangular finite element with local remeshing for the large strain analysis of axisymmetric solids. *Computer Methods in Applied Mechanics and Engineering*, *198*(2), 332-343.